metals

MDPI

Article

Laser Preheating for Hot Crack Reduction in Direct Metal Deposition of Inconel 738LC

Fabian Soffel [1,*], Konrad Papis [1], Markus Bambach [2] and Konrad Wegener [3]

[1] Inspire AG, Technoparkstrasse 1, 8005 Zürich, Switzerland; papis@inspire.ethz.ch
[2] Advanced Manufacturing Laboratory, ETH Zürich, Technoparkstrasse 1, 8005 Zürich, Switzerland; mbambach@ethz.ch
[3] Institute of Machine Tools and Manufacturing, ETH Zürich, Leonhardstrasse 21, 8092 Zürich, Switzerland; wegener@iwf.mavt.ethz.ch
* Correspondence: soffel@inspire.ethz.ch; Tel.: +41-44-633-0849; Fax: +41-44-633-1492

Abstract: Welding of precipitation-hardenable nickel-based super alloys that contain large amounts of Al and Ti is challenging due to their high susceptibility to hot cracking. For metal additive manufacturing (AM) by powder bed fusion (PBF) or direct metal deposition (DMD), various welding process adjustments may prevent the formation of cracks. The aim of this study is the development and experimental characterization of a laser preheating process for DMD of Inconel 738LC. Metallographic cross-sections of multiple test specimens were analyzed to quantify the effect of initial substrate temperature, specimen geometry, deposition parameters, and scanning strategy on the resulting crack density. The results show that increased substrate temperature by laser preheating and reduced specimen size leads to crack-free deposited structures. Therefore, the proposed preheating process may be applied for part fabrication or repair by DMD to reduce or even completely prevent the risk of hot cracking.

Keywords: additive manufacturing; direct metal deposition; preheating; isothermal welding; super alloy; Inconel; hot cracking

Citation: Soffel, F.; Papis, K.; Bambach, M.; Wegener, K. Laser Preheating for Hot Crack Reduction in Direct Metal Deposition of Inconel 738LC. *Metals* **2022**, *12*, 614. https://doi.org/10.3390/met12040614

Academic Editors: Vera Popovich and Aleksander Lisiecki

Received: 11 February 2022
Accepted: 28 March 2022
Published: 2 April 2022

1. Introduction

Metal additive manufacturing (AM) typically refers to processes based on welding, such as laser powder bed fusion (PBF-L), electron beam powder bed fusion (PBF-EB), and direct metal deposition (DMD). Powder bed fusion describes a two-step process principle whereby, first, a mechanical system distributes a powder layer and, second, a heat source locally melts the material [1–4]. Direct metal deposition is a single-step process in which carrier gas continuously transports powder into the melt pool [5–7]. This characteristic of DMD is especially advantageous for repair applications or the fabrication of larger parts because it enables the deposition on arbitrary-shaped structures [8]. Precipitation-strengthened nickel-based super alloys are widely used in the energy and aerospace industries due to their excellent corrosion and high-temperature properties [9,10]. However, large amounts of Al and Ti that are added to generate $Ni_3(Al,Ti)$ γ'-precipitates lead to poor weldability [11,12], and hot crack formation significantly limits AM of these alloys. The high susceptibility to hot cracking of this alloy system was shown, for example, for Inconel 738LC, CM247LC, K417G, and Waspaloy [13–16]. DebRoy et al. [17] stated the need to deeper understand various hot cracking phenomena, and several previous studies focused on their qualitative and quantitative description.

The main mechanisms for crack formation in nickel-based super alloys during welding and metal AM processes are solidification and liquation cracking. According to Kou [18], solidification cracks occur in the fusion zone during the terminal stage of solidification, while liquation cracks develop in the partially melted zone due to grain boundary liquation. Xu et al. [19] investigated crack formation in DMD of Inconel 738 and men-

tioned that the control of crack formation requires a clarification of its mechanism. However, Chauvet et al. [20] remarked that the distinction between the two main crack mechanisms is not straightforward in practice because both require the presence of liquid films, and the intrinsic heat treatment during metal AM may change the crack morphology. Rickenbacher et al. [13] processed Inconel 738LC by PBF-L and found intergranular microcracks with lengths in the range of 50 µm to 250 µm. Adegoke et al. [14] found comparable crack lengths for PBF-L of alloy 247LC. Grange et al. [21] investigated the microcrack surface for Inconel 738LC processed by PBF-L more in detail by bending a test specimen up to failure and analyzing the crack surface by scanning electron microscopy (SEM). They observed a regularly oriented dendritic microstructure and reported lack of liquid metal feeding in the terminal solidification stage as an indicator of solidification cracking.

For direct metal deposition of γ′-strengthened nickel-based super alloys, several studies detected crack propagation over multiple deposited layers that led to significantly larger crack lengths. Liu et al. [16] used DMD for the repair of Waspaloy components and found crack propagation and liquation along grain boundaries. Liu et al. [15] observed multiple crack mechanisms for DMD with alloy K417G and identified liquation cracking as the most common type due to the formation of low-melting eutectics along the grain boundaries. When re-heated above the eutectic temperature during deposition of the following layers, these eutectics may form liquid films that, in combination with contraction, lead to intergranular cracks with a high potential for crack propagation over multiple deposited layers. Without process adjustments, Seidel et al. [22] found crack propagation throughout the entire height of a multilayer structure deposited by DMD with a γ′-strengthened nickel-based super alloy. Therefore, adjustments of the AM process seem to be mandatory to avoid crack formation.

The prevention of hot cracking for this alloy system is possible by several adjustments before and during the welding process. For example, alloy modifications and substrate preheating are upstream measures, while induction-assisted welding and deposition parameter variations are applied during the process. Engeli et al. [23] processed different batches of Inconel 738LC by PBF-L and found that reduced contents of Si lead to lower crack densities. Based on this finding, the same author [24] proposed a modified alloy with reduced contents of Si and Zr and showed a reduction of crack density by a factor of 6. Similarly, Griffiths et al. [25] investigated a modified alloy CM247LC with a reduced amount of Hf for two PBF-L process conditions and, compared to a non-modified alloy, the crack density decreased by 36% and 75%, respectively. Chiang and Chen [26] used laser deposition welding with Inconel 738 powder and inductive preheating at approximately 800 °C to obtain crack-free butt joints. For welding of γ′-strengthened nickel-based super alloys, Stueber et al. [27] proposed to maintain the weld area and its adjacent region at a ductile temperature during the solidification of the weld in the range of between 760 °C and 1093 °C, which is in between the aging and incipient melting temperature of the alloy. Such an isothermal welding process was realized by Xu et al. [28] for Inconel 738LC by inductive substrate heating up to 1050 °C and DMD, which led to crack-free deposited structures. Similarly, Seidel et al. [22] obtained crack-free CM247LC structures by induction-assisted DMD. Several studies focused on the variation of deposition parameters. Cloots et al. [29] varied the scanning speed in PBF-L of Inconel 738LC and found a significantly reduced crack density for higher speed levels. In contrast, Ramakrishnan and Dinda [30] found a reduced cracking susceptibility for lower scanning speeds for DMD of the same alloy. Lee et al. [31] investigated different scanning strategies for PBF-EB of Inconel 738LC to fabricate airfoil structures and found reduced crack formation and lower distortion for modified scan patterns that presumably led to more uniform stress distributions. Based on the findings of previous studies, preheating and isothermal welding seem to have the largest potential to fabricate crack-free structures by DMD of Inconel 738LC. However, as described by Cortina et al. [32], many modern DMD systems are combined machine tools with five-axis configurations. Due to these configurations, the integration of an additional heating system as demonstrated by Seidel et al. [22] and Xu et al. [28] may be technically

challenging and not economically feasible, such that novel concepts should be evaluated. Therefore, preheating by the laser of the DMD system in combination with additional process optimizations might be an alternative solution for the crack-free deposition of γ′-strengthened nickel-based super alloys within such machine tools.

The aim of this study is to develop a laser preheating process and to investigate its potential for direct metal deposition of Inconel 738LC in combination with other process adjustments. These adjustments include a variation of the specimen geometry, deposition parameters, and scanning strategy. In this paper, Section 2 describes the experimental procedure; Section 3 presents and discusses the results of the quantitative and qualitative crack analysis; and, finally, Section 4 summarizes the main conclusions.

2. Materials and Methods

A five-axis GF HPM 450 U (Georg Fischer AG, Schaffhausen, Switzerland) direct metal deposition (DMD) and milling machine with an Ambit S5 laser processing system from HMT (Hybrid Manufacturing Technologies, Midlands, UK) was used for part fabrication. The laser system included an IPG YLR-1000-MM-WC (IPG Photonics Corporation, Oxford, MA, USA) fiber laser with a wave length of 1070 nm and a water-cooled DMD processing head with coaxial powder feeding. The working distance of the processing head was set at 9.0 mm, which resulted in an approximate melt pool width of 2.2 mm. Argon was selected as local shielding, powder carrier, and nozzle protection gas and supplied at flow rates of 8 L/min, 6 L/min, and 4 L/min, respectively. Table 1 lists the chemical composition of the Inconel 738LC metal powder. The substrates, on which the specimens were deposited, were 1.4404 stainless steel plates with a length of 50.0 mm, a width of 25.0 mm, and a thickness of 8.0 mm.

Table 1. Chemical composition of the Inconel 738LC metal powder.

Element	Al	C	Co	Cr	Mo	Nb	Ni	Si	Ta	Ti	W	Zr	Others
wt.%	3.44	0.10	8.54	16.10	1.72	0.83	Bal.	0.09	1.73	3.41	2.55	0.06	<0.19

Figure 1 shows the specimen geometries and the investigated scanning vector orientations. Cuboids with edge lengths a = 5 mm, a = 10 mm, and a = 15 mm were chosen as sample geometry to investigate the effect of part size on crack formation. They were deposited with a 0°/90° bidirectional raster scanning strategy, where the orientation of the parallel scanning vectors is rotated by 90° after each layer. To investigate the effect of a modified scanning pattern, a wall geometry with a height H of 15.0 mm, a length L of 14.0 mm, and a width W of 7.0 mm, as illustrated in Figure 1 (right), was selected. For this wall geometry, the conventional 0°/90° and a modified 80°/100° bidirectional raster scanning strategy were applied. Table 2 details the experimental conditions for the specimen fabrication.

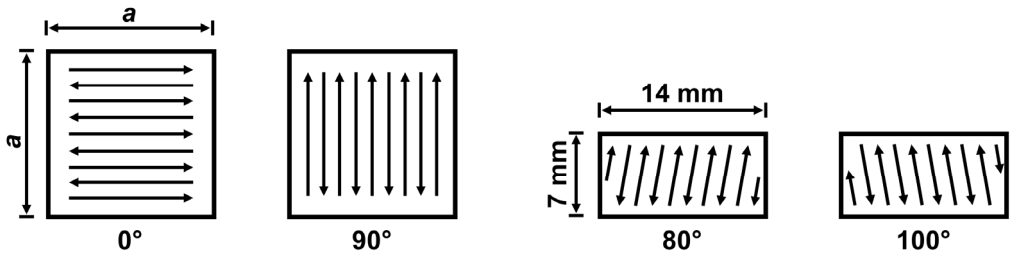

Figure 1. Specimen geometries and scanning vector orientations.

Table 2. Experimental conditions for the specimen fabrication.

Specimen	$L \times W \times H$ [mm^3]	Parameter Set [-]	Scanning [-]	Substr. Temp. [°C]
S1	5 × 5 × 5	P1	0°/90°	20
S2	5 × 5 × 5	P2	0°/90°	20
S3	5 × 5 × 5	P3	0°/90°	20
S4	5 × 5 × 5	P4	0°/90°	20
S5	10 × 10 × 10	P1	0°/90°	20
S6	10 × 10 × 10	P2	0°/90°	20
S7	10 × 10 × 10	P3	0°/90°	20
S8	10 × 10 × 10	P4	0°/90°	20
S9	15 × 15 × 15	P1	0°/90°	20
S10	15 × 15 × 15	P2	0°/90°	20
S11	15 × 15 × 15	P3	0°/90°	20
S12	15 × 15 × 15	P4	0°/90°	20
S13	15 × 15 × 15	P3	0°/90°	975
S14	14 × 7 × 15	P3	0°/90°	20
S15	14 × 7 × 15	P3	0°/90°	975
S16	14 × 7 × 15	P3	80°/100°	20
S17	14 × 7 × 15	P3	80°/100°	975

Table 3 lists the selected process parameter combinations P1 to P4. The laser power was set constant to 1000 W, and scanning speed and powder flow rate were varied on two levels each. These parameters were selected based on previous unpublished work of the authors, where comparable low scanning speeds and powder flow rates led to lowest porosity. For all specimens, the hatching distance d between the scanning vectors was 1.1 mm and the theoretical layer height Δz was between 0.54 and 0.84 mm, based on single layer experiments with the respective process parameter combinations.

Table 3. Processing parameter sets.

Parameter Set	Laser Power [W]	Scanning Speed [mm/min]	Powder Flow Rate [g/min]
P1	1000	250	2.0
P2	1000	300	2.0
P3	1000	250	2.5
P4	1000	300	2.5

For a variation of the initial substrate temperature, a laser preheating process was applied as illustrated in Figure 2. The working distance was raised to 50 mm and the scanning speed to 3000 mm/min to avoid local substrate melting. The machine table was tilted to 40° to reduce back reflection, and a rectangular scanning pattern was followed for 50 repetitions and a duration of 100 s. For the final 10 repetitions, the powder feeding was activated to obtain a stable material flow before the deposition started. An Optris PI 1M infrared camera (Optris GmbH, Berlin, Germany) with a spectral range between 0.85 µm to 1.1 µm was used to measure the substrate temperature during the developed preheating process.

Metallographic preparation and image analysis were conducted for the quantitative assessment of the cracking phenomena. The specimens were cut with a water-cooled abrasive grinding disc, embedded in thermoplastic resin, ground with SiC foils up to grit 4000, and polished with 3 µm and 1 µm diamond suspension. In order to fully reveal the cracks, an etchant consisting of 100 mL H_2O, 100 mL HCl, and 5 g Cu_2Cl (Kalling II) was applied. Full cross-section images were taken on a Keyence VHX 5000 digital microscope (Keyence, Osaka, Japan) in both polished and etched condition, and the length of each crack was analyzed using ImageJ software (version 1.51p, ImageJ, National Institutes of Health, Bethesda, MD, USA). The measurement uncertainty for the quantitative crack

analysis was assumed to be 5%. A selected specimen was examined with a Zeiss EVO 10 scanning electron microscope (SEM, Carl Zeiss AG, Jena, Germany) equipped with an Oxford Instruments X-Max^N detector for energy-dispersive X-ray spectroscopy (EDS, Oxford Instruments, Abingdon, UK).

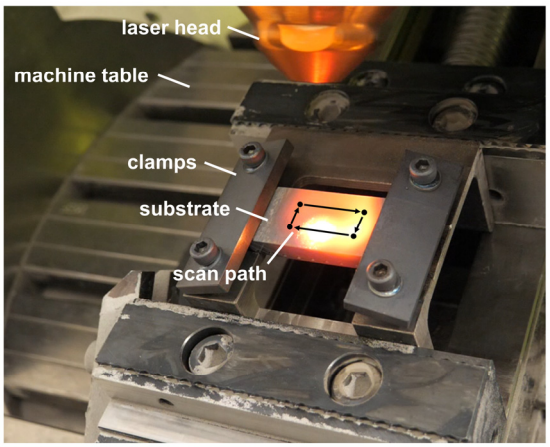

Figure 2. Experimental setup for the laser preheating process.

3. Results and Discussion

Figure 3 displays the crack densities for varying cube sizes and processing parameters. The crack density significantly increases for larger specimen geometries. While the specimens with the smallest edge length a = 5 mm are nearly crack-free, the crack densities for the larger cubes rise to between 0.08 and 0.20 mm/mm^2 for a = 10 mm and to between 0.45 and 0.57 mm/mm^2 for a = 15 mm. This corresponds to an average increase in crack density by 348% from edge length a = 10 mm to a = 15 mm. This finding may be of interest for repair applications, where the deposit size may be influenced by removing more or less material around the area of the defect prior to the deposition process.

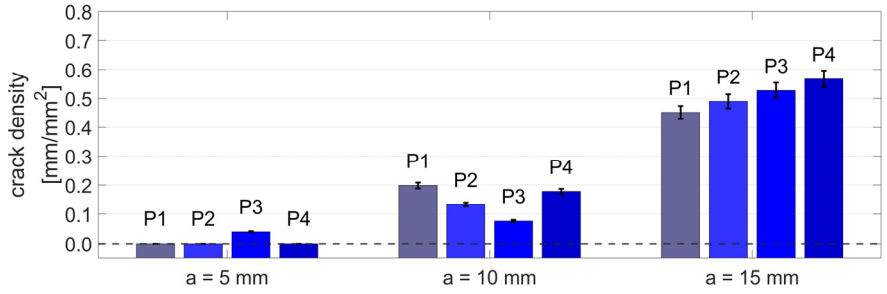

Figure 3. Crack density for specimens S1 to S12 with varied cube geometry and process parameter sets P1 to P4. The initial substrate temperature was constant around 20 °C. Error bars represent 5% measurement uncertainty.

There is no consistent tendency regarding the effect of processing parameters. The volumetric energy input

$$e_v = \frac{P}{vd\Delta z} \quad (1)$$

with laser power P, scanning speed v, hatching distance d, and theoretical layer height Δz for the tested conditions varied only between 270 and 374 J/mm^3, which presumably led to similar melt pool and thermal boundary conditions. Therefore, the narrow levels of the selected deposition parameters seem to inhibit a clear statement about the process parameter influence. In contrast, the specimen geometry significantly affects both the melt pool and thermal boundary conditions. For smaller specimens, a larger amount of heat

accumulation occurs, because of the shorter scanning vectors and the lower amount of conductive heat transfer through the already deposited material. This heat accumulation may prevent cracking by three mechanisms: first, as discussed by Grange et al. [21], the healing of cracks by the deposition of the following layer is supported by melt pools that are larger and longer in the liquid state. Second, the increased base temperature leads to lower cooling rates during solidification and less segregation of low-melting phases at the grain boundaries, which is, according to Chen et al. [33], especially important for the prevention of liquation cracks. Third, as described by Stueber et al. [27], the lower cooling rates result in a lower magnitude of shrinking stresses, which is effective for the reduction of all types of hot cracking modes in nickel-based super alloys. According to these findings, there seems to be the potential to further reduce the crack densities of as-deposited alloy 738LC by increased substrate temperatures and optimized scanning strategies with shorter scanning vector lengths.

Figure 4 shows the temperature of the substrate material during the developed laser preheating process determined by three measurements with an infrared camera. The substrate temperature increases to above 1100 °C and exponentially decays after preheating for 102.75 s when the laser is turned off. For the following experiments, the deposition starts 5.70 s after the end of preheating. Therefore, the initial substrate temperature before the deposition start can be determined from the temperature profiles at a processing time of 108.45 s. The determined substrate temperatures at this time for the three tests are 967.1 °C, 976.7 °C, and 984.3 °C, respectively. Hence, an average temperature of 975 °C can be indicated as the initial substrate temperature for the following experiments with laser preheating.

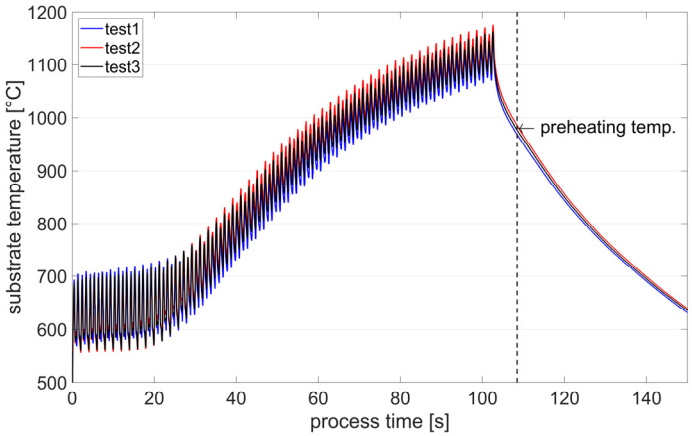

Figure 4. Temperature profiles of the developed laser preheating process. The initial substrate temperature for the following experiments was determined at a processing time of 108.45 s, as indicated by the dashed line.

Figure 5 illustrates the effect of initial substrate temperatures and scanning strategies on the resulting crack densities for two different specimen geometries. For the cuboid geometry with an edge length a = 15 mm, laser preheating of the substrate reduces the crack density to 0.10 mm/mm^2, compared to 0.53 mm/mm^2 for the deposition at room temperature. For the wall geometry with a cross section of 14.0 mm × 7.0 mm, the scanning vector length is 14.0 mm and 7.0 mm for orientations of 0° and 90°, respectively. For the modified 80°/100° scanning strategy, as visualized in Figure 1 (right), the maximum vector length is shortened to 7.1 mm, which is expected to reduce the amount of residual stress. However, the measured crack density without preheating for both scanning strategies has the same value of 0.08 mm/mm^2. Hence, the residual stress for both conditions is larger than the local material strength, and the optimized deposition pattern does not prevent cracks for this geometry. In contrast, the application of the laser preheating process to the wall geometry led to crack-free structures, presumably due to the lower levels of shrinkage

stresses as described by Stueber et al. [27]. Therefore, laser preheating has a larger potential for crack prevention compared to process parameter and scanning strategy optimizations because it reduces residual stress to a greater extend.

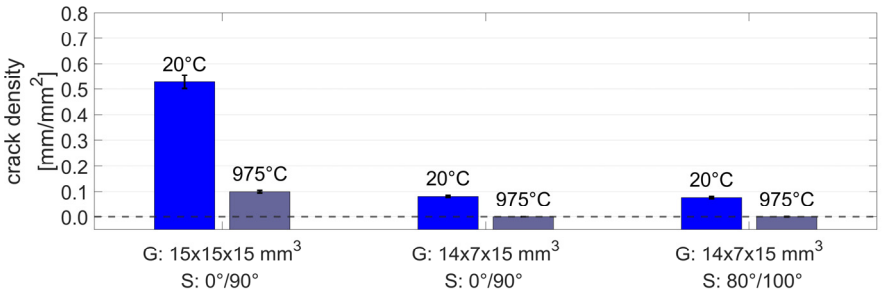

Figure 5. Crack density for different specimen geometries G, scanning strategies S, and initial substrate temperatures. Error bars represent 5% measurement uncertainty.

Figure 6 compares the cross section and crack density analysis for the cuboid geometries with different initial substrate temperatures (specimens S11 and S13). Without laser preheating, a large number of cracks appear throughout the specimen, except for some regions in the bottom and the top layer. In the bottom layer, the lower crack density may be related to the dilution with the substrate material 1.4404, which may lead to a smaller amount of Al- and Ti-enriched low-melting phases. In the top layer, the absence of large cracks strongly indicates that the main cracking mechanism is liquation cracking, which occurs in the heat-affected zone of the already deposited material underneath the latest deposited layer with a high potential for crack propagation over several layers. For the specimen with preheated substrate, there is a crack-free zone in the lower half of the structure. In this zone, the preheating process led to the highest initial substrate temperatures and lowest cooling rates. Hence, the amount of residual stress and the segregation of low-melting phases were reduced to the greatest extend in this lower region. In the upper regions, heat losses due to conduction, convection, and radiation during the process gradually reduced the temperature of the substrate and deposited structure over time. Consequently, residual stress and segregation increased, such that crack formation could not be completely prevented for this specimen geometry. This is similar to the findings of Chauvet et al. [20] for the deposition of a γ'-hardenable nickel alloy by electron beam powder bed fusion (PBF-EB) with preheating, where the 30 mm high test structure was crack-free only for the first 12 mm. Therefore, an initial preheating process alone may prevent hot cracking only for small specimen geometries. Further reduction of the crack density for larger structures may be possible by intermediate preheating to maintain a higher temperature of the already deposited structure. Alternatively, a laser remelting process as described by Leech [34] and as developed in a previous work by the authors [35] may be applied in between each layer.

Figure 7 illustrates the microstructure and the details of specimen S13 in etched condition. The microstructure shows a pattern of directional solidification and large, elongated grains. This is similar to the findings of Xu et al. [28] for preheating temperatures of 800 °C and 900 °C, where hot cracking could not be prevented, whereas for a preheating temperature of 1050 °C the fraction of equiaxed grains significantly increased and the deposit was free of cracks. The magnification of the crack in Figure 7 shows that the crack is located along the boundaries of multiple grains. Hence, grain boundary liquation may have caused the formation of this crack.

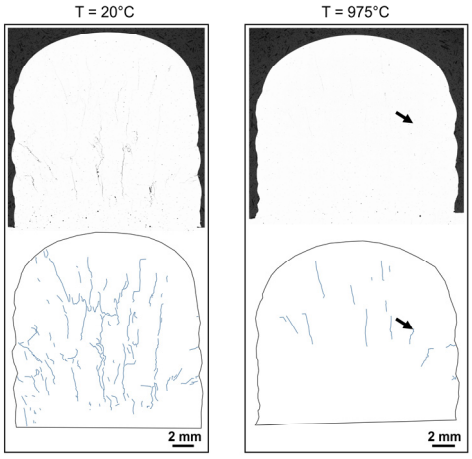

Figure 6. Polished cross-sections (**top**) and crack visualization (**bottom**) for cubes with 15 mm edge length fabricated without (**left**) and with (**right**) laser preheating to increase the initial substrate temperature T. The arrows show the location of an exemplary crack that is illustrated at higher magnification in the following figure.

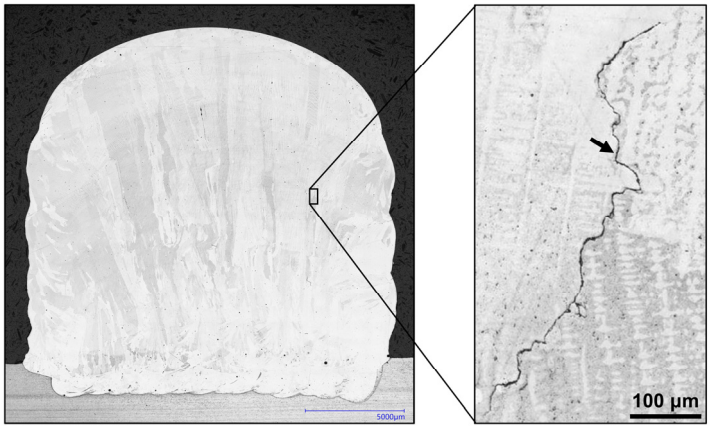

Figure 7. Optical microscope image of specimen S13. The arrow indicates the location that is shown at a higher magnification in Figure 8.

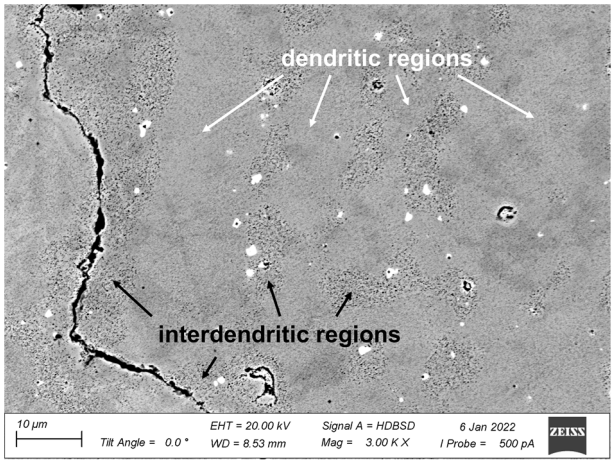

Figure 8. Backscatter electron image of a cracked grain boundary and its surroundings.

Figure 8 shows a backscatter electron image of a section of the previously shown crack and its surrounding dendritic microstructure. Within the interdendritic regions, block-shaped particles with a size of between 0.2 and 2.0 µm are present that appear

white in the image. Energy-dispersive X-ray spectroscopy (EDS) revealed an enrichment of Ta and Ti in the interdendritic regions and identified the white particles as mixed carbides with enhanced contents of C, Cr, Ta, Ti, and W. As described by Ojo et al. [36], the high susceptibility to liquation cracking of alloy 738 is related to the liquation of γ′ precipitates, and resolidified γ-γ′ eutectic products may be found in the crack vicinity. Similarly, Chen et al. [33] confirmed the presence of γ-γ′ colonies in the HAZ of alloy 738 welds. Hence, the enrichment of Ti in the interdentritic regions at the crack surroundings indicate that grain boundary liquation may be a possible explanation for crack formation in the present study.

Figure 9 displays further details of a cracked area at higher magnification, and Table 4 lists the chemical composition detected by EDS for selected points of interest. Due to the inaccuracy of EDS for low atomic weights, the measured contents of carbon and oxygen may significantly deviate from the actual content of the specimen and are for comparison purposes only. Point 1 represents the bulk material, where the chemical composition is similar to the raw powder material. The enrichment in C, Nb, Ta, Ti, and W identifies the white particles (Point 2 and 3) as mixed carbides. Within the crack, increased levels of oxygen are presumed to be associated with oxides deposited in the terminal stage of solidification or residual components from the metallographic preparation.

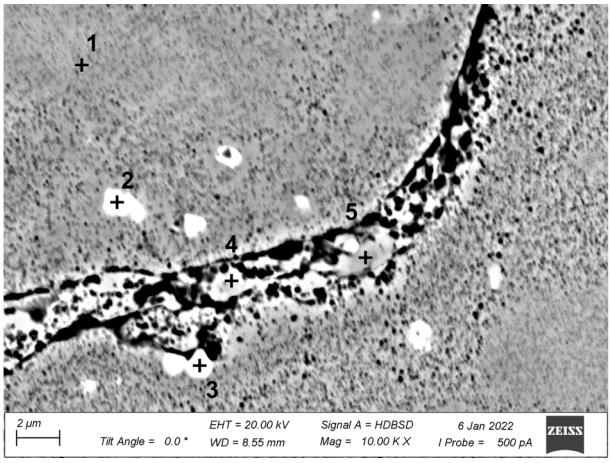

Figure 9. Backscatter electron image of a cracked region and selected points for EDS analysis.

Table 4. EDS results in wt. % of the points illustrated in Figure 8.

Element	Al	C	Co	Cr	Nb	Ni	O	Ta	Ti	W
Point 1	3.1	4.4	8.4	16	0.5	57.6	0	1.9	2.6	3.3
Point 2	0.3	12.5	1.8	4.6	9.3	11.0	0	25.5	25.3	6.0
Point 3	2.6	9.0	2.6	6.1	10.3	18.3	7.1	21.1	14.3	4.6
Point 4	3.1	5.0	7.8	15.2	0.8	55.5	2.2	2.1	3.3	3.0
Point 5	3.0	4.6	7.7	15.1	0.7	55.5	2.9	2.3	3.5	2.7

The main limitations of this study are related to the statistical uncertainty of the experimental results as each condition was measured only once and only one type of material was used. Since each process parameter combination was fabricated and analyzed only once, no statement about the repeatability of the measurements is possible. Hence, future studies may include the analysis of multiple specimens for each condition for the statistical validation of the results. Furthermore, future studies may validate laser preheating and DMD for other brittle materials, such as Mo-Si-B based alloys, for which Higashi and Yoshimi [37] showed a high susceptibility to crack formation.

4. Conclusions

Within this study, a laser preheating process was developed for direct metal deposition (DMD) of precipitation-hardenable nickel-based super alloys. The process was successfully validated for Inconel 738LC, and the main conclusions are as follows:

- The crack formation significantly depends on the size of the deposited structure and the solidification conditions because smaller structures heat up and experience low levels of thermal stress. While the smallest cubes with 5 mm edge length were nearly free of cracks, the crack density increased from between 0.08 and 0.20 mm/mm^2 to between 0.45 and 0.57 mm/mm^2 for the edge lengths 10 mm and 15 mm, respectively.
- The variation of scanning speed, powder flow rate, and scanning pattern did not significantly affect the crack formation within the analyzed conditions of this study.
- Laser preheating strongly reduced the crack density for all tested conditions. Structures of dimension 14 mm $\times$ 7 mm $\times$ 15 mm built on a substrate at room temperature showed a crack density of 0.08 mm/mm^2, while the deposition on preheated substrates led to microstructures without detected cracks. For the largest analyzed specimens, laser preheating led to a reduction in crack density by a factor of 5.3.
- The proposed process is implementable on existing DMD machines and does not require any additional hardware. Therefore, the laser preheating process appears to be economically feasible for the repair of super alloy components by DMD.

Author Contributions: Conceptualization, F.S. and K.W.; methodology, F.S. and K.P.; validation, F.S. and K.P.; formal analysis, F.S.; investigation, F.S. and K.P.; resources, M.B. and K.W.; writing—original draft preparation, F.S.; writing—review and editing, K.P., M.B. and K.W.; visualization, F.S.; supervision, M.B. and K.W.; project administration, F.S. and K.W.; funding acquisition, M.B. and K.W. All authors have read and agreed to the published version of the manuscript.

Funding: The authors would like to acknowledge the support by the funding agency Innosuisse (grant number 25498) and the companies GF Machining Solutions, GF Precicast, and ABB Schweiz AG, Turbocharging.

Institutional Review Board Statement: Not applicable.

Informed Consent Statement: Not applicable.

Data Availability Statement: The datasets generated during and/or analyzed during the current study are available from the corresponding author on reasonable request.

Acknowledgments: The authors would like to thank Knut Krieger, Daniel Eisenbarth, and Arthur Riesen for their assistance within this study.

Conflicts of Interest: The authors declare no conflict of interest.

References

1. DebRoy, T.; Wei, H.L.; Zuback, J.S.; Mukherjee, T.; Elmer, J.W.; Milewski, J.O.; Beese, A.M.; Wilson-Heid, A.; De, A.; Zhang, W. Additive manufacturing of metallic components—Process, structure and properties. *Prog. Mater. Sci.* **2018**, *92*, 112–224. [CrossRef]
2. Xiong, Z.; Li, Z.; Sun, Z.; Hao, S.; Yang, Y.; Li, M.; Song, C.; Qiu, P.; Cui, L. Selective laser melting of NiTi alloy with superior tensile property and shape memory effect. *J. Mater. Sci. Tech.* **2019**, *35*, 2238–2242. [CrossRef]
3. Elahinia, M.; Shayesteh Moghaddam, N.; Taheri Andani, M.; Amerinatanzi, A.; Bimber, B.A.; Hamilton, R.F. Fabrication of NiTi through additive manufacturing: A review. *Prog. Mater. Sci.* **2016**, *83*, 630–663. [CrossRef]
4. Smelov, V.G.; Sotov, A.V.; Murzin, S.P. Particularly Selective Sintering of Metal Powders by Pulsed Laser Radiation. *Key Eng. Mater.* **2016**, *685*, 403–407. [CrossRef]
5. Mazumder, J. Laser-aided direct metal deposition of metals and alloys. In *Laser Additive Manufacturing*; Woodhead Publishing: Sawston, UK, 2017; pp. 21–53. [CrossRef]
6. Wirth, F.; Wegener, K. A physical modeling and predictive simulation of the laser cladding process. *Addit. Manuf.* **2018**, *22*, 307–319. [CrossRef]
7. Wirth, F.; Arpagaus, S.; Wegener, K. Analysis of melt pool dynamics in laser cladding and direct metal deposition by automated high-speed camera image evaluation. *Addit. Manuf.* **2018**, *21*, 369–382. [CrossRef]
8. Rettberg, R.; Kraenzler, T. Hybrid manufacturing: A new additive manufacturing approach for closed pump impellers. In *Industrializing Additive Manufacturing*; Springer: Cham, Switzerland, 2021; pp. 146–159. [CrossRef]

9. Hosseini, E.; Popovich, V.A. A review of mechanical properties of additively manufactured Inconel 718. *Addit. Manuf.* **2019**, *30*, 100877. [CrossRef]
10. Murzin, S.P.; Kazanskiy, N.L.; Stiglbrunner, C. Analysis of the Advantages of Laser Processing of Aerospace Materials Using Diffractive Optics. *Metals* **2021**, *11*, 963. [CrossRef]
11. Zhong, M.; Sun, H.; Liu, W.; Zhu, X.; He, J. Boundary liquation and interface cracking characterization in laser deposition of Inconel 738 on directionally solidified Ni-based superalloy. *Scr. Mater.* **2005**, *53*, 159–164. [CrossRef]
12. Montazeri, M.; Ghaini, F.M. The liquation cracking behavior of IN738LC superalloy during low power Nd:YAG pulsed laser welding. *Mater. Charact.* **2012**, *67*, 65–73. [CrossRef]
13. Rickenbacher, L.; Etter, T.; Hövel, S.; Wegener, K. High temperature material properties of IN738LC processed by selective laser melting (SLM) technology. *Rapid Prototyp. J.* **2013**, *19*, 282–290. [CrossRef]
14. Adegoke, O.; Andersson, J.; Brodin, H.; Pederson, R. Influence of Laser Powder Bed Fusion Process Parameters on Voids, Cracks, and Microhardness of Nickel-Based Superalloy Alloy 247LC. *Materials* **2020**, *13*, 3770. [CrossRef] [PubMed]
15. Liu, S.; Yu, H.; Wang, Y.; Zhang, X.; Li, J.; Chen, S.; Liu, C. Cracking, Microstructure and Tribological Properties of Laser Formed and Remelted K417G Ni-Based Superalloy. *Coatings* **2019**, *9*, 71. [CrossRef]
16. Liu, D.; Lippold, J.C.; Li, J.; Rohklin, S.R.; Vollbrecht, J.; Grylls, R. Laser Engineered Net Shape (LENS) Technology for the Repair of Ni-Base Superalloy Turbine Components. *Metall. Mater. Trans. A* **2014**, *45*, 4454–4469. [CrossRef]
17. DebRoy, T.; Mukherjee, T.; Milewski, J.O.; Elmer, J.W.; Ribic, B.; Blecher, J.J.; Zhang, W. Scientific, technological and economic issues in metal printing and their solutions. *Nat. Mater.* **2019**, *18*, 1026–1032. [CrossRef] [PubMed]
18. Kou, S. Predicting Susceptibility to Solidification Cracking and Liquation Cracking by CALPHAD. *Metals* **2021**, *11*, 1442. [CrossRef]
19. Xu, J.; Lin, X.; Guo, P.; Dong, H.; Wen, X.; Li, Q.; Xue, L.; Huang, W. The initiation and propagation mechanism of the overlapping zone cracking during laser solid forming of IN-738LC superalloy. *J. Alloys Compd.* **2018**, *749*, 859–870. [CrossRef]
20. Chauvet, E.; Kontis, P.; Jägle, E.A.; Gault, B.; Raabe, D.; Tassin, C.; Blandin, J.-J.; Dendievel, R.; Vayre, B.; Abed, S.; et al. Hot cracking mechanism affecting a non-weldable Ni-based superalloy produced by selective electron Beam Melting. *Acta. Mater.* **2018**, *142*, 82–94. [CrossRef]
21. Grange, D.; Bartout, J.D.; Macquaire, B.; Colin, C. Processing a non-weldable nickel-base superalloy by Selective Laser Melting: Role of the shape and size of the melt pools on solidification cracking. *Materialia* **2020**, *12*, 100686. [CrossRef]
22. Seidel, A.; Finaske, T.; Straubel, A.; Wendrock, H.; Maiwald, T.; Riede, M.; Lopez, E.; Brueckner, F.; Leyens, C. Additive Manufacturing of Powdery Ni-Based Superalloys Mar-M-247 and CM 247 LC in Hybrid Laser Metal Deposition. *Metall. Mater. Trans. A* **2018**, *49*, 3812–3830. [CrossRef]
23. Engeli, R.; Etter, T.; Hövel, S.; Wegener, K. Processability of different IN738LC powder batches by selective laser melting. *J. Mater. Process. Tech.* **2016**, *229*, 484–491. [CrossRef]
24. Engeli, R.; Etter, T.; Meidani, H. Gamma Prime Precipitation Strengthened Nickel-Base Superalloy for Use in Powder Based Additive Manufacturing process. U.S. Patent US 2017/0021453 A1, 26 January 2017.
25. Griffiths, S.; Ghasemi Tabasi, H.; Ivas, T.; Maeder, X.; De Luca, A.; Zweiacker, K.; Wróbel, R.; Jhabvala, J.; Logé, R.E.; Leinenbach, C. Combining alloy and process modification for micro-crack mitigation in an additively manufactured Ni-base superalloy. *Addit. Manuf.* **2020**, *36*, 101443. [CrossRef]
26. Chiang, M.F.; Chen, C. Induction-assisted laser welding of IN-738 nickel–base superalloy. *Mater. Chem. Phys.* **2009**, *114*, 415–419. [CrossRef]
27. Stueber, R.; Milidantri, T.; Tadayon, M. Welding High-Strength Nickel Base Superalloys. U.S. Patent US5374319A, 28 September 1990.
28. Xu, J.; Lin, X.; Guo, P.; Hu, Y.; Wen, X.; Xue, L.; Liu, J.; Huang, W. The effect of preheating on microstructure and mechanical properties of laser solid forming IN-738LC alloy. *Mat. Sci. Eng. A* **2017**, *691*, 71–80. [CrossRef]
29. Cloots, M.; Uggowitzer, P.J.; Wegener, K. Investigations on the microstructure and crack formation of IN738LC samples processed by selective laser melting using Gaussian and doughnut profiles. *Mater. Des.* **2016**, *89*, 770–784. [CrossRef]
30. Ramakrishnan, A.; Dinda, G.P. Direct laser metal deposition of Inconel 738. *Mat. Sci. Eng. A* **2019**, *740–741*, 1–13. [CrossRef]
31. Lee, Y.S.; Kirka, M.M.; Ferguson, J.; Paquit, V.C. Correlations of cracking with scan strategy and build geometry in electron beam powder bed additive manufacturing. *Addit. Manuf.* **2020**, *32*, 101031. [CrossRef]
32. Cortina, M.; Arrizubieta, J.I.; Ruiz, J.E.; Ukar, E.; Lamikiz, A. Latest Developments in Industrial Hybrid Machine Tools that Combine Additive and Subtractive Operations. *Materials* **2018**, *11*, 2583. [CrossRef]
33. Chen, K.-C.; Chen, T.-C.; Shiue, R.-K.; Tsay, L.-W. Liquation Cracking in the Heat-Affected Zone of IN738 Superalloy Weld. *Metals* **2018**, *8*, 387. [CrossRef]
34. Leech, P.W. Laser surface melting of a complex high alloy steel. *Mat. Des.* **2014**, *54*, 539–543. [CrossRef]
35. Soffel, F.; Lin, Y.; Keller, D.; Egorov, S.; Wegener, K. Laser Remelting Process Simulation and Optimization for Additive Manufacturing of Nickel-Based Super Alloys. *Materials* **2022**, *15*, 177. [CrossRef] [PubMed]
36. Ojo, O.A.; Richards, N.L.; Chaturvedi, M.C. Contribution of constitutional liquation of gamma prime precipitate to weld HAZ cracking of cast Inconel 738 superalloy. *Scr. Mater.* **2004**, *50*, 641–646. [CrossRef]
37. Higashi, M.; Yoshimi, K. Electron beam surface melting of MoSiBTiC alloys: Effect of preheating on cracking behavior and microstructure evolution. *Mater. Des.* **2021**, *209*, 110010. [CrossRef]